Raman Lidar Measurements During the International H_2O Project. II. Instrument Comparisons and Case Studies

D. N. Whiteman, B. Demoz, P. Di Girolamo, J. Comer, I. Veselovskii, K. Evans, Z. Wang, D. Sabatino, G. Schwemmer, B. Gentry, R.-F. Lin, E. Browell, R. Ferrare, S. Ismail, J. Wang

To be submitted to Journal of Atmospheric and Oceanic Technology

Abstract

The NASA/GSFC Scanning Raman Lidar (SRL) participated in the International H_2O Project (IHOP) that occurred in May and June, 2002 in the midwestern part of the U. S. The SRL system configuration and methods of data analysis were described in part I of this paper. In this second part, comparisons of SRL water vapor measurements and those of chilled mirror radiosonde and LASE airborne water vapor lidar are performed. Two case studies are presented; one for daytime and one for nighttime. The daytime case study is of a convectively driven boundary layer event and is used to characterize the SRL water vapor random error characteristics. The nighttime case study is of a thunderstorm-generated cirrus cloud case that is studied in it's meteorological context. Upper tropospheric humidification due to precipitation from the cirrus cloud is quantified as is the cirrus cloud ice water content and particle depolarization ratio. These detailed cirrus cloud measurements are being used in a cirrus cloud modeling study.

1 Table Of Contents

2 Introduction

The International H_2O Project (IHOP), which occurred in the Midwestern U.S. between May 13 - June 25, 2002, was the largest meteorological field campaign ever held in the United States [Weckworth et. al., 2004]. The instrumentation used during IHOP included seven research aircraft carrying three water vapor lidars and one wind lidar, mobile radar systems for storm-chasing, and a ground-based site in the western panhandle of Oklahoma that included the NASA/Goddard Space Flight Center (GSFC) Scanning Raman Lidar (SRL). The goal of IHOP was to improve forecasting of convective storm systems and precipitation. The first part of this paper [Whiteman et. al., 2005a] (hereafter referred to as part I) focussed on the instrumentation of the SRL during IHOP and the data analysis technique used. In part II, comparisons of SRL water vapor measurements with other instruments will be presented followed by daytime and nighttime case studies that permit the error characteristics of the system to be quantified and illustrate the diurnal measurement capabilities.

3 SRL operations during IHOP

During the first several days of IHOP, numerous instruments including the SRL were not fully operational thus delaying the effective onset of the experiment. Once operations began in earnest, a total of approximately 225 hours of vertically pointing SRL data were acquired during IHOP. A chart of the operational periods of the SRL during IHOP is shown in figure 1. Most of the measurements were concentrated during late morning to early evening hours when convection was most likely to develop. There were several early morning jet experiments that also took place. A complete listing of the IHOP measurement periods and

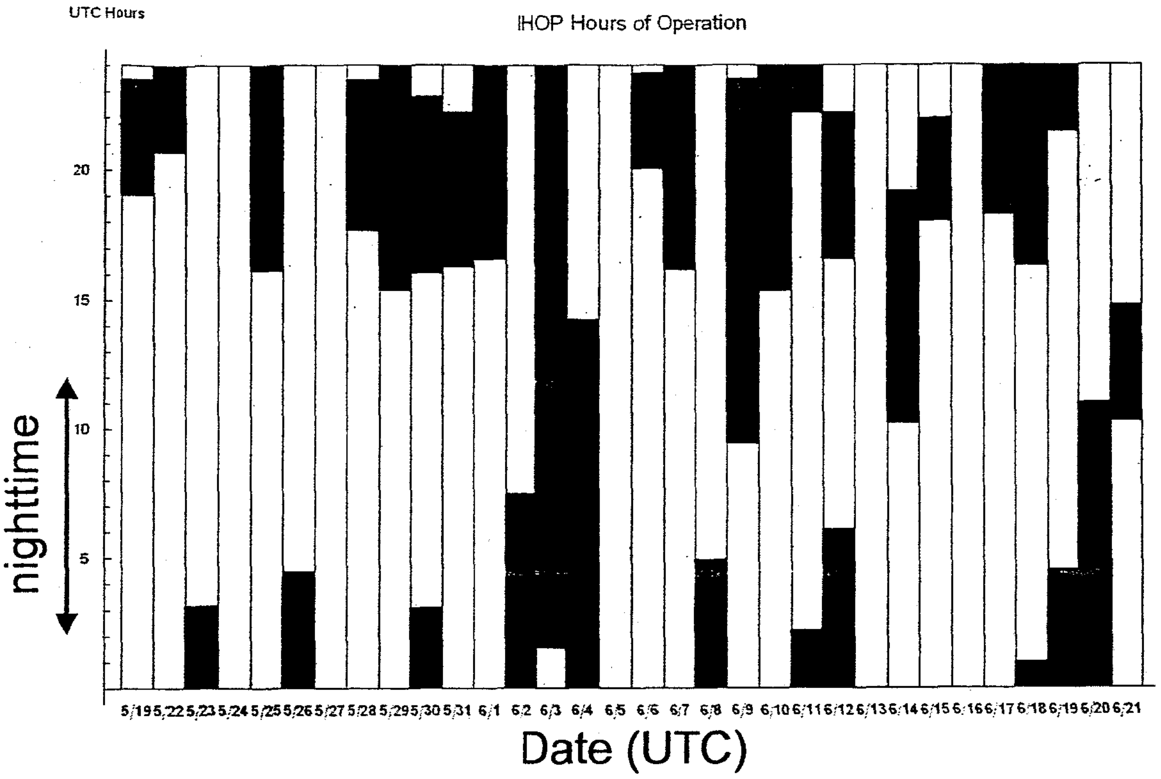

Figure 1: The SRL hours of operation as a function of day during IHOP. Most measurements were concentrated during the daytime when convection was most likely to develop. Several early morning low level jet experiments also were performed.

objectives can be seen at http://www.ofps.ucar.edu/ihop/catalog/missions.html.

4 Comparison of SRL Water Vapor Measurements with Other Sensors

Atmospheric water vapor measurements were simultaneously performed between the ground-based SRL, the airborne Lidar Atmospheric Sensing Experiment (LASE) system [Browell and Ismail, 1995] [Browell et. al., 1997] and the NCAR Reference Sonde (SW) [Wang et. al., 2003] during IHOP. Example comparisons of SRL and these other profilers will now be presented along with the statistics of all comparisons.

4.1 LASE

Comparison of SRL and LASE water vapor data was possible on four distinct days: 30 May, 3 June, 9 June and 14 June, 2002. Only those cases characterized by distances smaller than 20 km between the closest point of LASE overpass and Homestead were considered. This provided a total of 24 possible comparisons between SRL and LASE. However, comparisons for 14 June were discarded because of an operational problem with LASE that precluded an independent comparison with SRL. For this reason, the number of comparisons considered here is 12. Comparisons are based on 10-minute averaging of SRL data and 1-minute averaging of LASE data.

Comparisons between SRL and LASE are shown for three overpasses on May 30 in figure 2. The measurements of the two lidars show good general agreement for these bright daytime measurements. Larger deviations between the two instruments are occasionally found at the top of the boundary layer, where the effect of spatial inhomogeneities (as manifested by dry air mixing down from above the boundary layer) may be larger.

The mean comparison of SRL and LASE profiles is shown in figure 3. The differences between the profiles is generally less than 10% below 2 km and less than 20% below 3 km.

In order to better quantify these profile comparisons, mean deviations between SRL and LASE were computed after interpolating SRL data to LASE data heights. For each day, the bias and root mean square

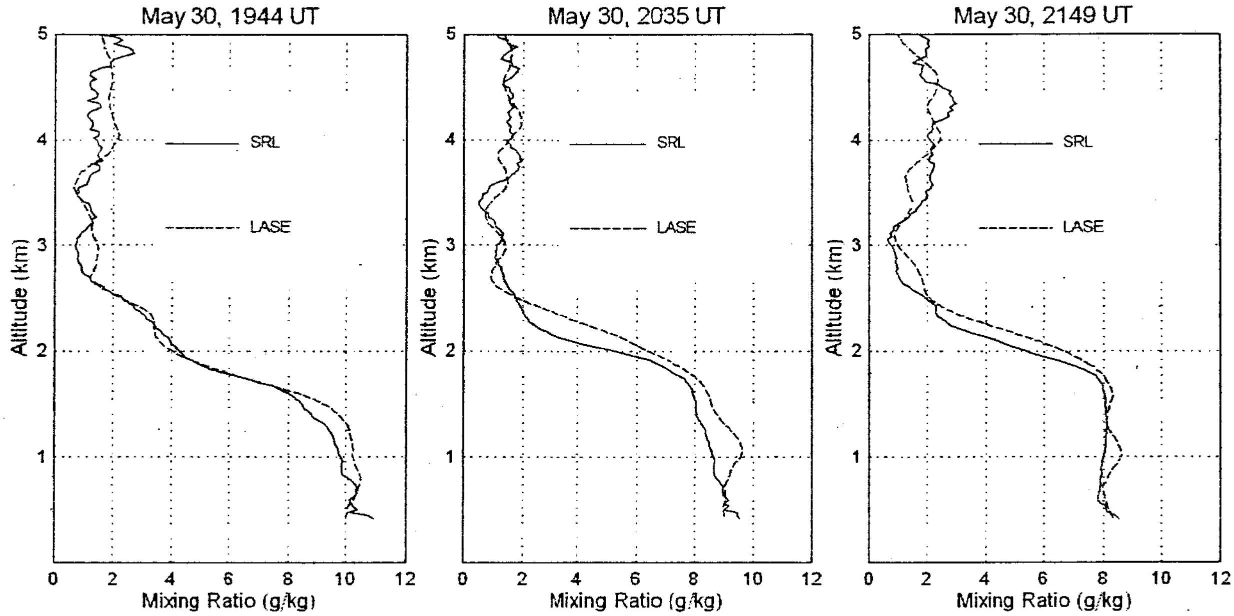

Figure 2: Example comparisons of three overflights of the SRL site by the LASE airborne water vapor lidar on May 30, 2002. The SRL and LASE data use 10 and 1 minute average respectively. Note that all profiles are acquired in the daytime.

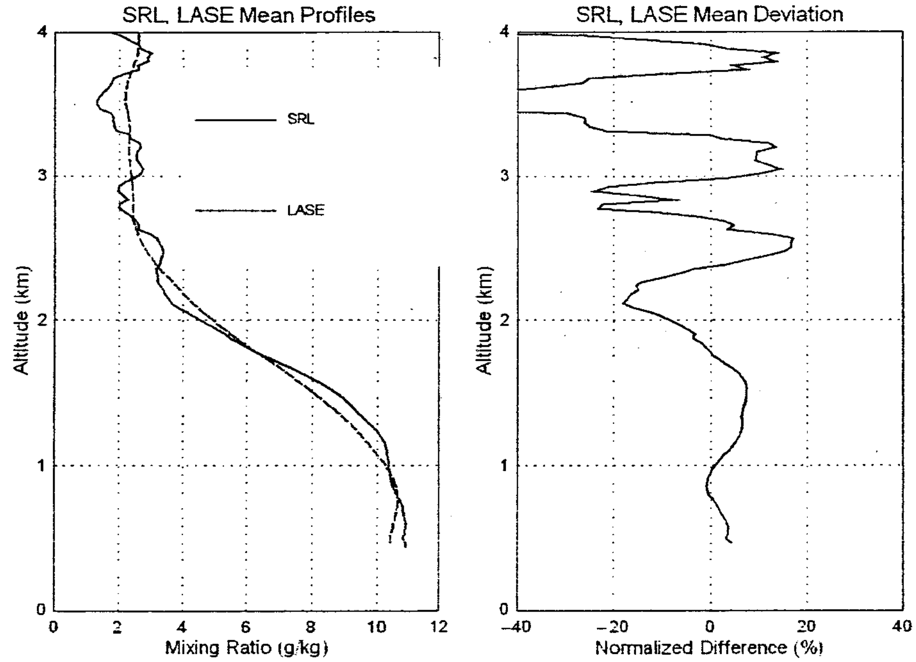

Figure 3: Mean profile and deviation comparisons between SRL and LASE during the IHOP experiment. The mean bias of the data plotted is -3.1% (SRL drier) while the mean RMS deviation is 11.9%. The integrated precipitable water between 0.4 and 4.0 km of the two mean profiles agreed to better than 1%.

(RMS) deviation between the two sensors were computed using equations 1 and 2,

$$BIAS(\%) = \frac{\sum_{i=1}^{N}(SRL_i - LASE_i)}{\sum_{i=1}^{N}(\overline{n_i})} \tag{1}$$

$$RMS(\%) = \frac{\sqrt{\frac{1}{N}\sum_{i=1}^{N}(SRL_i - LASE_i)^2}}{\frac{1}{N}\sum_{i=1}^{N}(\overline{n_i})} \tag{2}$$

where i is the index of height and $\overline{n_i}$ represents the average between SRL and LASE.

The average RMS deviation between SRL and LASE was found to be 11.9 % between 0.4 and 4.0 km, while the average BIAS deviation between SRL and LASE was -3.1 % between 0.4 and 4.0 km. The integrated precipitable water over this same altitude region was 0.8% higher for the SRL mean profile than for LASE. Comparisons were not performed to altitudes greater than 4 km since these measurements occured mostly during the daytime when elevated solar backgrounds reduced the SRL signal-to-noise above 4 km.

4.2 NCAR Reference Sonde

Comparisons between SRL and the NCAR Reference Sonde, which combines a SnowWhite chilled mirror sensor and a Vaisala RS-80 radiosonde [Wang et. al., 2003], have been also performed. Four distinct sonde launches were considered on 28 May, 9 June, 18 June, 20 June 2002. Once again, the SRL data were averaged over a 10-minute period for these comparisons. Water vapor mixing ratios for the reference sonde have been calculated using pressure information from simultaneous Vaisala RS80 radiosonde since pressure

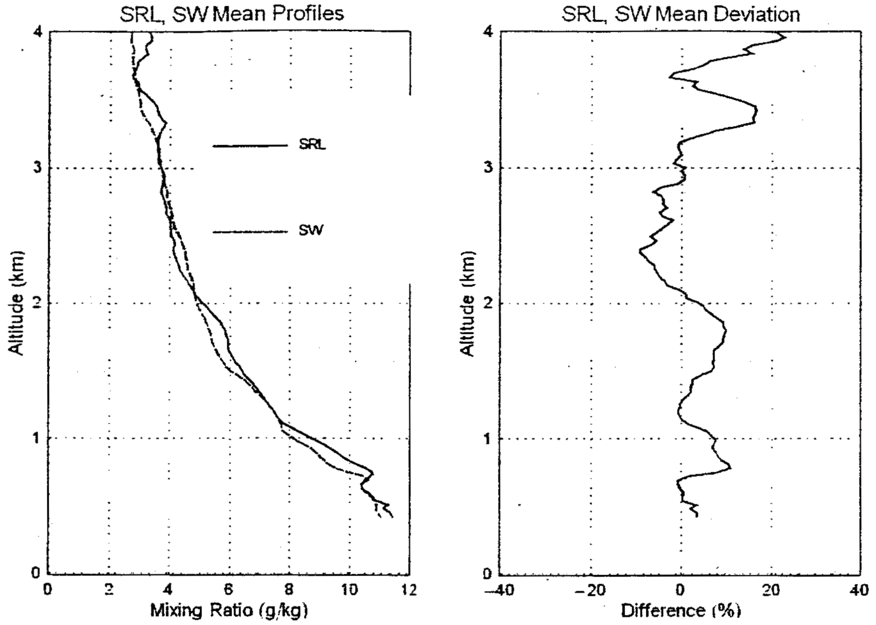
SRL, SW Mean Profiles

SRL, SW Mean Deviation

Figure 4: Mean profile and deviation between the SRL and the NCAR reference sensor that includes SnowWhite (SW) and Vaisala RS-80H. The mean bias was 3.0% (SRL wetter) and mean RMS difference was 7.0% for the region plotted. The integrated precipitable water between 0.4 and 4.0 km of the mean SRL profile was 2.7% higher than that of the reference sonde.

information from the reference sonde itself was considered to not be reliable. In order to compute deviations needed for the estimates of BIAS and random error, SRL data have been interpolated to the reference sonde data heights. Figure 4 shows the mean profile and percent deviation comparisons of SRL and the reference sonde. The profiles show good general agreement with deviations of less than 10% to an altitude beyond 3 km.

For each of the four cases mentioned above, root mean square deviation and bias between the two sensors have been computed using expressions similar to equations 1 and 2 over the height range of 0.4 to 4.0 km.

The average RMS deviation between SRL and the Reference Sonde was found to be 7.1% , while the average BIAS deviation between SRL and the reference sonde was 3.1 %. The integrated precipitable water over this same altitude range was 2.7% higher in the SRL mean profile than in the reference sonde. As in the case with LASE, comparisons were not performed to altitudes greater than 4 km due to the influence of daytime solar background.

5 Daytime and Nighttime Case Studies

The challenge for Raman lidar measurements is particularly large during the daytime when the large solar background makes accurate measurement of the relatively weak Raman signals more difficult. Therefore the measurement characteristics of a non-solar blind water vapor Raman lidar will differ considerably between daytime and nighttime. SRL measurements from two IHOP intensive observations periods will now be presented in order to illustrate the daytime and nighttime measurement capability of the SRL as configured for IHOP.

5.1 Daytime convective boundary layer measurements

On 22-23 May 2002, the IHOP forecasting team predicted that convection would initiate in the Oklahoma Panhandle, near where the SRL was located. The SRL water vapor mixing ratio measurements from this period are shown on the left in figure 5. The water vapor mixing ratio data are displayed from 0.3 to 5 km and over a range of mixing ratio values of 0-15 g kg^{-1} for a period of ~6.5 hours. Moving window averages in the vertical and temporal domains have been applied. The temporal moving window for the water vapor data was 3 minutes while the spatial moving windows were as follows: 0-1km: 90 meters, 1-2km: 150 m, 2-3km: 210m, 3-4km: 270m, >4km: 330m. The resulting water vapor temporal resolutions, determined by the half-power point in a Fourier spectral analysis, is approximately 2 minutes while the vertical resolution varies approximately as follows: 0-1 km : 60m, 1-2 km : 100m, 2-3 km : 150m, 3-4 km : 180m, >4 km : 210m.

On this day, the height of the daytime boundary layer was observed to grow from approximately 2.4 km at 2030 UTC to ~3.5 km at 2400 UTC. Sunset occurred at approximately 0130 UTC on May 23 (indicated as 2530 UTC in the figure) after which time advection of air from the south influenced the local water vapor environment more strongly leading to the condition of moist low level air capped by dry air above 1.5 km. The vertical stripes in the water vapor field represent convective plumes of water vapor. The white stripes that extend above the top of the boundary layer at, for example, ~2300 UTC and ~2400 UTC, are due to noise created by the attenuation of the laser beam by convectively generated clouds that formed at the top of the boundary layer. The simultaneously acquired aerosol scattering ratio image is presented in the bottom of figure 5 using the same temporal and spatial resolution as in the water vapor mixing ratio image to illustrate the same convective plumes in the aerosol field and to denote the locations of clouds that formed at the top of the boundary layer. For more details on this case, see reference [Demoz et. al., 2004].

5.1.1 Daytime random error characterization

The dryline case of May 22 shown in figure 5 has been used to characterize the random errors in the SRL water vapor mixing ratio data. For photon counting data, errors can be calculated assuming Poisson statistics using equation 6 from part I [Whiteman et. al., 2005a], to be referred to as the water vapor error equation. However, as discussed in part I, the water vapor mixing ratio measurements in general use a combination of photon counting and analog measurements. In general, calculating statistics on a single profile of analog

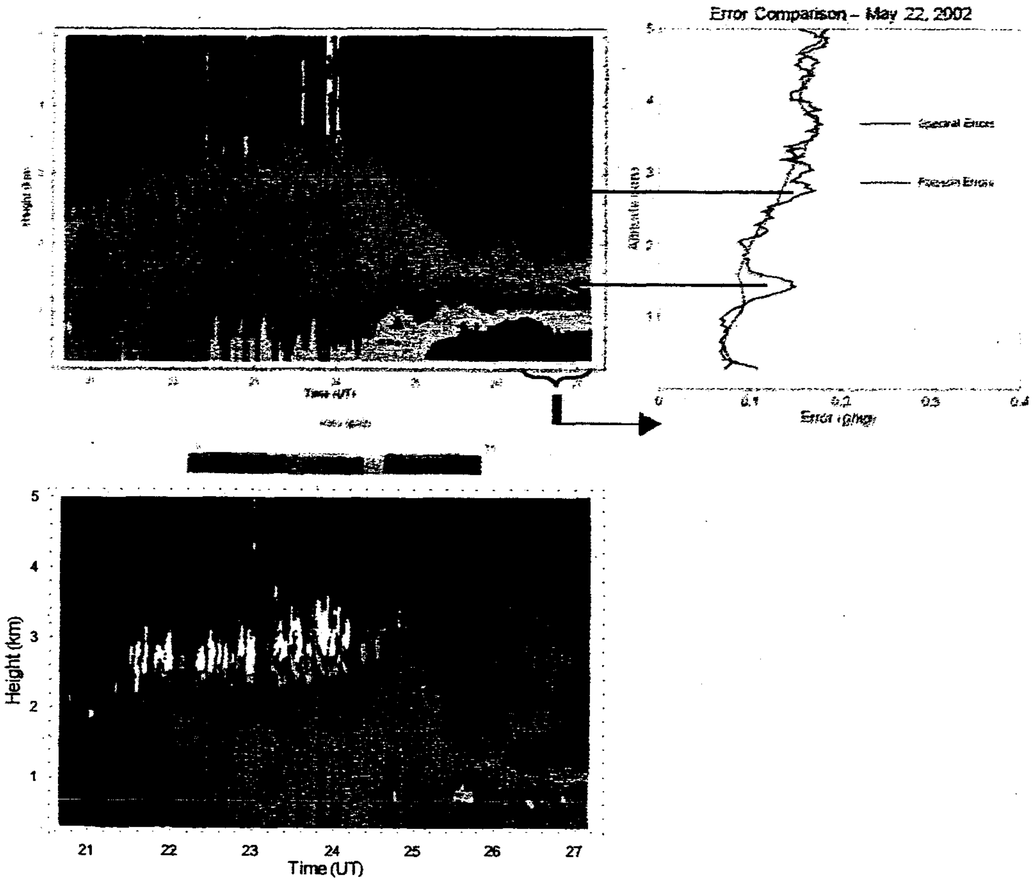

Figure 5: Upper left: water vapor mixing ratio time series during a dryline passage on May 22, 2002. Convectively driven plumes of water vapor are visible in the image. Lower left: corresponding aerosol scattering ratio plot that shows the convectively driven clouds at the top of the boundary layer. Upper right: comparison of errors using Fourier analysis and assuming Poisson error propagation during the last 50 minutes of data in the image (noted by the red brace). There is good agreement between the two techniques except in the regions noted by the red errors where significant atmospheric variation exists.

data requires that the square of the signal for each laser shot that goes into a summed profile be maintained [Whiteman et. al., 1992]. That information is not maintained in the current data acquisition electronics so another approach to determining errors in the analog data is required. The method used here is to first convert the analog signal to a virtual countrate scale using the glue coefficients determined through a regression analysis. The virtual countrate corresponding to the analog signal is used for the S terms in the water vapor error equation and the background determined from the photon counting data are used for the B terms. The implicit assumption is that the analog data converted to a virtual countrate scale behave according to Poisson statistics.

This method of determining the errors has been tested by comparing the results of the water vapor error equation with errors determined using spectral analysis techniques where the noise floor in a Fourier power spectrum [Senff et. al., 1994] [Linné et. al., 2000] is determined as a function of height. If a portion of data is used when the atmosphere is stable, i.e. where the real atmospheric variation is less than variations introduced by counting statistics, then the noise determined by this Fourier technique can be used to quantify the instrument noise floor. The upper right panel of figure 5 shows the comparison of the Poisson and spectrally determined random errors for the last 50 minutes of the measurement period (denoted by the horizontal brace on the time axis of the water vapor image). In order to improve the statistics of this comparison, the data have been used at their raw resolution (1 minute temporal and 30 meter spatial) instead of the smoothed resolution displayed in the image. In the final 50 minute segment of the water vapor mixing ratio image, analog data are used for the water vapor signal between 0.3 and approximately 2.0 km and for the nitrogen signal from 0.3 to 5.5 km. Therefore, the water vapor mixing ratio is calculated using exclusively analog data below approximately 2.0 km for this 50 minute segment. Above 2.0 km, the mixing ratio is determined using photon counting data for the water vapor and analog data for the nitrogen. The plot in figure 5 shows that the two methods of determining the variance in the signal agree well except for two altitude ranges between 1.2 - 1.6 km and 2.6 - 3.2, both indicated by horizontal arrows, where the spectrally determined variance exceeds that determined by Poisson statistics. The lower altitude range corresponds to the top of the nocturnal boundary layer (confirmed by potential temperature analysis from radiosonde) while the upper altitude range indicates the location of the residual layer. The increased atmospheric variability at these locations leads to larger variance in the spectral quantification of errors since the Fourier technique is quantifying both real atmospheric variation as well as variation due to the counting statistics. Therefore, this example illustrates that the Fourier and Poisson techniques for calculating errors agree well except in regions of increased atmospheric variability thus supporting the assumption that the technique of calculating errors from the converted analog data assuming Poisson statistics is justified. It also demonstrates that this error comparison technique can be used to discern transition regions in the atmosphere.

The analysis of figure 5 validates the use of Poisson statistics to determine the random component of the errors in the water vapor mixing ratio calculation. Figure 6 now presents a comparison of how the errors determined using Poisson statistics varied during the May 22-23, 2002 dataset. Using the smoothed resolution presented in figure 5, the random error was calculated at three times in the dataset: 21.1, 23.5, 26.4 UTC. (The latter time indicates 2.4 UTC on May 23, 2002). The first two of these measurements were in bright daytime conditions while the last was in full darkness. The random errors of the water vapor mixing ratio measurements for these three times are shown in 6.

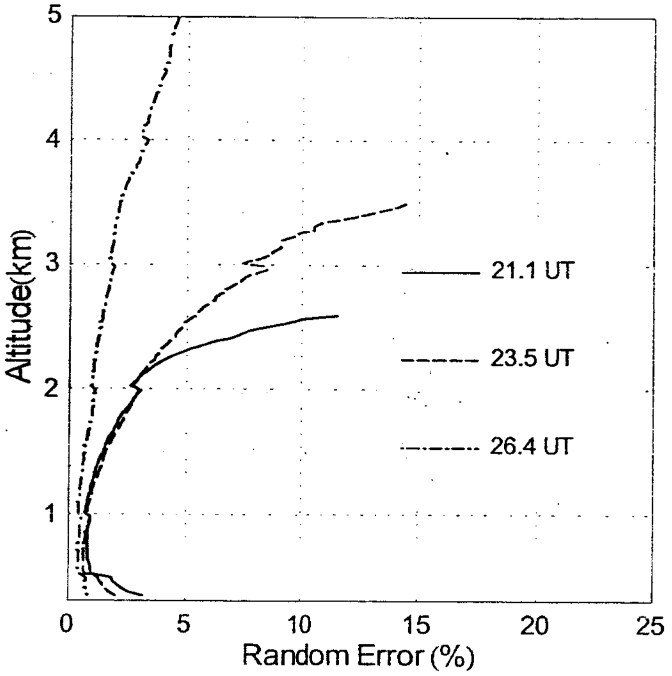

Figure 6: Random error in the SRL water vapor mixing ratio measurements on May 22, 2002. The random error remains below 10% in the boundary layer using 2 minute temporal and 60-200m spatial resolution.

These random error quantifications along with the boundary layer heights observed in figure 5 indicate that under all conditions, the random error in the mixing ratio measurement remains below 10% throughout the boundary layer at 2 minute temporal and 60 - 200 meter spatial resolution. During the daytime, the random errors increase steeply above the boundary layer where the water vapor content drops rapidly. However, under nighttime conditions, the random error does not exceed 10% below ~6 km. These high-resolution water vapor measurements permit boundary layer convective processes to be studied throughout the diurnal cycle as further described in reference [Demoz et. al., 2004].

5.2 June 19-20, 2002 Bore and cirrus cloud event - Upper tropospheric measurements

In section 5.1, it was demonstrated that the full utilization of the narrow band, narrow field-of-view technique permits convective processes to be studied in the daytime boundary layer. Narrowing the spectral band and the field-of-view of the lidar system also enhances upper tropospheric water vapor measurements at night. This will now be demonstrated for the case of June 19-20, 2002, which was used for the regression analysis performed in part I [Whiteman et. al., 2005a].

The extended set of SRL measurements acquired on June 19-20, 2002 revealed the atmosphere to possess a rich set of waves, or bores, in the water vapor field [Flamant et. al., 2003] as indicated by the ovals on the water vapor image in figure 2 of part I [Whiteman et. al., 2005a]. The bore activity was generated by outflow from a developing thunderstorm complex that was generally to the north of the SRL location. At approximately 0630 UTC on June 20, the strongest bore event (indicated by the oval on the lower right of the water vapor image) observed during the measurement period occurred at an altitude between 0.5 and 1.0 km. The oscillations in the moisture field at ~3.5 km, also indicated by an oval, are likely due to the upward thrust of energy from this event lower in the atmosphere. The overlying cirrus cloud field, created by anvil outflow from the thunderstorm to the north that was also the source of the bore outflow, can be seen in the aerosol scattering ratio image shown in figure 7. Notice that wave structure is also observed in the lower of the two scattering layers seen in this figure. Possible causes of this wave structure will be discussed later.

The potential temperature from 2 radiosonde launches is plotted on the figure. The potential temperature is nearly constant in the intense scattering region toward the top of the upper cloud layer. This is interpreted as indicating a well-mixed region in the upper levels of the cirrus clouds that decreases in thickness over the measurement period. We hypothesize that the well-mixed region is where cirrus particle generation is occurring and where particle sizes are small. As the cirrus cloud evolves, it begins to precipitate producing the fall-streaks that are present in the scattering ratio image. The generating region also decreases in vertical extent while the base of the cloud lowers. The falling ice crystals, which typically are large in size, evaporate in the dry upper troposphere and, as will be shown later, increase the relative humidity below the cloud.

5.2.1 Ice water content and particle radius retrievals

A newly developed Raman Lidar technique for quantifying cirrus cloud ice water content (IWC) and generalized particle diameter (Dge) [Wang et. al., 2004] makes use of simultaneous measurement of cirrus cloud scattering ratio and Raman scattering from ice. The technique was developed using measurements acquired at the U.S. Department of Energy Southern Great Plains Atmospheric Research Facility in northern Oklahoma where radar measurements were available for validation. This technique was used to retrieve IWC and particle size from these cirrus cloud measurements. The results are shown in panels c) and d) of figure 7. These retrievals show that the region of intense scattering between the altitudes of 12 -13 km and over the time interval of 0300 to 0500 UTC on June 20 (indicated as 27 and 29) is populated in general by small particles but high IWC consistent with this being the generating region for the cirrus particles. By contrast, later in the measurement period between 0800 and 1000 UTC, the retrieval of generally large particles in the 11 to 12 km altitude range and smaller particles above this is consistent with this being a region of cirrus precipitation.

5.2.2 Upper troposphere humidification

In order to study the influence of the sublimating cirrus particles on upper tropospheric humidity, the relative humidity with respect to ice (RH_{Ice}) was quantified at 2 hour intervals during the time of the evolving cirrus cloud where temperature profiles from radiosonde were used to calculate RH_{Ice} from the lidar mixing ratio. The times at which RH_{Ice} was quantified were 0400, 0600, 0800, 1000 UTC and are indicated by the color-coded arrows in the image shown in figure 7b. The vertical profiles of RH_{Ice} corresponding to the times indicated by the arrows are shown in figure 7a . Careful study of the figure shows that sub-cloud RH_{Ice} values approximately double over the period of the measurements likely due to sublimation of the precipitating ice crystals from the cloud. Also observed is approximately a factor of 4 increase in the mean RH_{Ice} at the altitude of the lower scattering layer.

5.2.3 Upper Tropospheric Water Vapor Random Error Characteristics

Figure 7 demonstrates the upper tropospheric water vapor measurement capability of the SRL during IHOP. The relative humidity profiles presented in figure 7 were analyzed using a routine that performs variable smoothing in both the spatial and temporal domain. The resulting vertical resolution of the data presented in figure 7 ranges from 60 meters at 7 km to 600 meters beyond 12 km. The procedure works as follows:

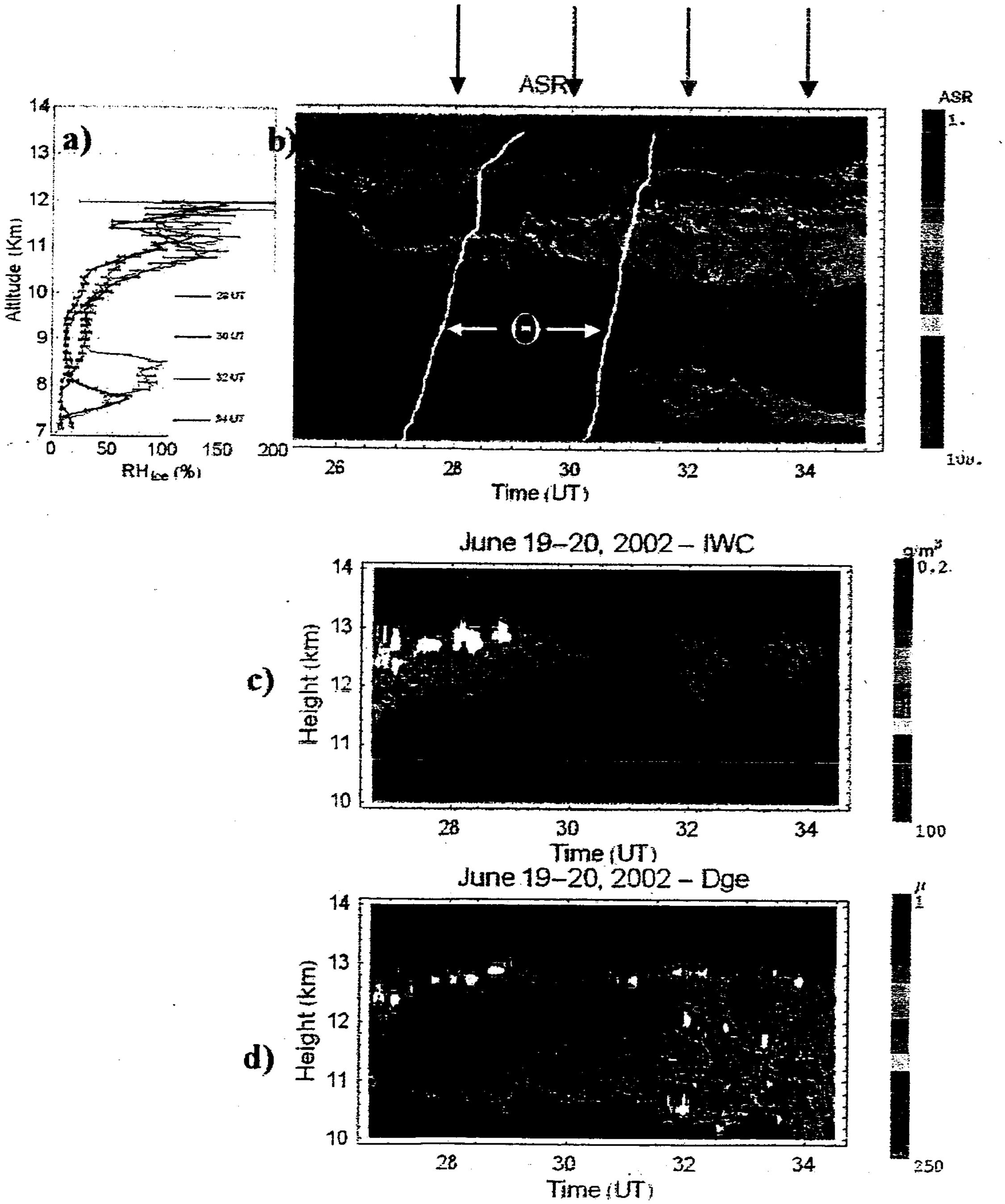

Figure 7: Upper right: time series of aerosol scattering ratio image of a cloud system involving two layers. The upper layer is a cirrus cloud due to outflow from a thunderstorm system to the north. The lower layer, which shows interesting oscilliations is studied further in the main text. Upper left: relative humidity with respect to ice calculated from SRL water vapor and radiosonde temperatures at two hour intervals during the development of the cloud system. Significant upper tropospheric humidification is observed due to cirrus precipitation. Ice super saturation is also observed inside the cloud. Middle and lower images: ice water content and generalized particle diameter retrievals using the newly developed retrieval [Wang et. al., 2004] that uses Raman scattering from ice along with the cloud scattering ratio.

the water vapor mixing ratio profiles are first vertically-smoothed to the desired resolution, then the routine sums the number of profiles required to maintain the random error below a fixed value, chosen here to be 10%. At higher altitudes, more profiles are required to maintain a random error of 10% or less. A maximum number of 59 profiles, one acquired each minute, was specified for summing. This method of analyzing the data permits higher resolution temporal features to be preserved in the lower altitudes of the profiles. On the left of figure 8, therefore, is shown the resulting random error as a function of altitude that is achieved using this routine. On the right is shown the number of profiles that have been included in the processed data shown in figure 7. Note that above some altitude, it was not possible to maintain less than 10% random error for the vertical resolution chosen. This altitude varies from ~11.5 km between 0400 and 0600 UTC to 9.5 km at 1000 UTC. The reduction in this altitude at the later times is due to the increased attenuation of the laser beam by the lower scattering layer seen in figure 7.

5.2.4 Investigation of wave structure in lower scattering layer

The oscillations in the lower scattering layer seen in b) of figure 7 suggest the possibility that energy from the bore event shown at the time/altitude of ~0630 UTC/~0.5 km in the water vapor image of figure 2 in part I has propagated upward to ~9 km and induced the oscillations seen in b) of figure 7. This possibility was studied by calculating the Scorer parameter, l_s^2 [Scorer 1949], which considers the balance between the atmospheric stability and wind shear as a function of altitude and can be used to identify regions of trapping for vertically propagating waves [Ralph et. al., 1997] [Shutts, 1997]. It is defined as

$$l_s^2 = \frac{N^2}{U^2} - \frac{1}{U}\frac{d^2U}{dz^2}$$

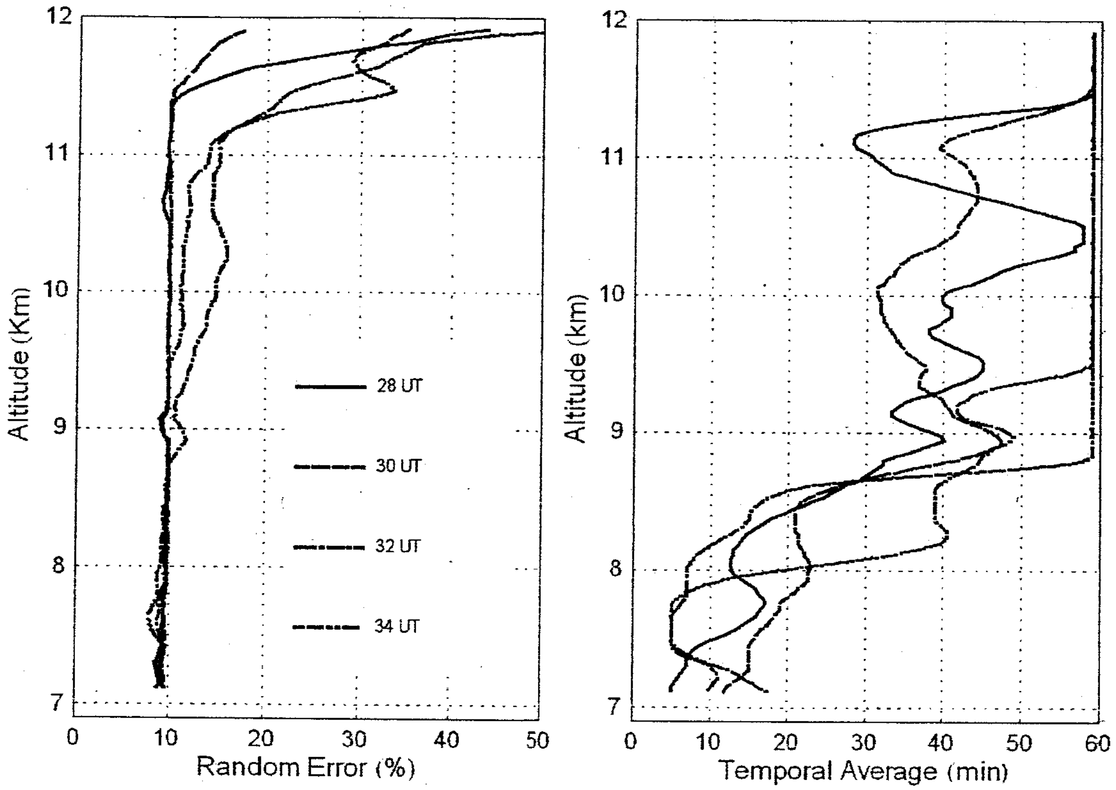

Figure 8: Left: random error in the relative humidity data displayed in figure 7. A variable smoothing routine is used that attempts to maintain less than 10% random error but does not permit more than 59 minutes of temporal smoothing. Right: the number of profiles used in the relative humidity profile as a function of altitude for the 4 profiles shown in figure 7.

where z is the vertical coordinate, N is the Brunt Vaisala frequency defined by

$$N^2 = \frac{g}{\theta_v}\frac{\partial\overline{\theta_v}}{\partial z}$$

$U(z)$ is the component of the horizontal wind in the x - direction. Disturbances can propagate vertically for $l_s^2 > 0$ and are trapped for $l_s^2 < 0$. The Scorer parameter calculated from radiosondes launched at 0602 and 0801 UTC (approximately 30 and 32 UTC on figure 7) from the Homestead site is shown on the left side of figure 9. The negative values of l^2 at approximately 3 km coupled with the near zero values of l^2 between 4 and 6 km do not support the hypothesis that upward propagating energy from the bore thrust observed at 0630 UTC and 0.5 km in figure 2 of part I was the source of energy for the oscillations observed in the lower scattering layer in figure 7. Furthermore, a careful examination of the image suggests that the oscillations in the lower cloud layer may have begun prior to the major bore thrust at 0630 UTC.

To investigate other possible explanations for the presence of waves in the lower scattering layer, consider the wind speed and direction data from the 0602 and 0801 UTC radiosondes shown on the right of figure 9. Large directional shear is observed in the wind field of figure 9 at the base of the cirrus outflow layer at ~11km consistent with the GOES satellite loop, which indicated that the outflow from the thunderstorm that produced the upper layer of cirrus clouds observed in figure 7 was generally from the north and then veered toward the east as the measurement period proceeded.

Within the generally westerly flow in the mid-troposphere, there still was significant variation in wind direction. The wind veered continuously from approximately 160^o to 300^o between the altitudes of 5 and 7 km. This implies the possibility of directional shear in the wind field within this altitude range. Considering that the Scorer analysis indicates that waves can vertically propagate in the altitude range of 6 - 8 km and

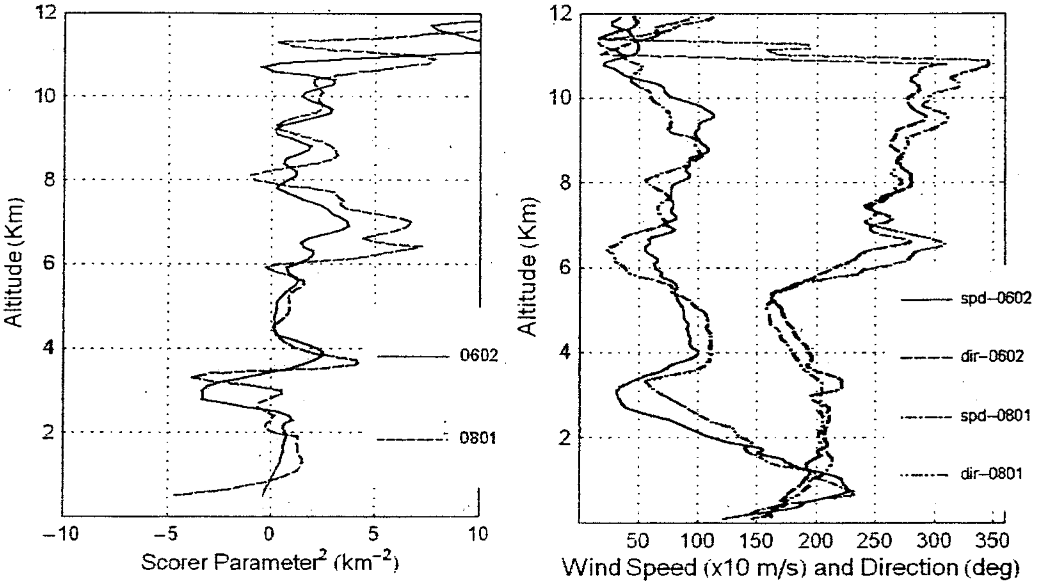

Figure 9: Left: the Scorer parameter calculated on June 20, 2002 using radiosondes launched at 0602 and 0801 UT from the Homestead site. Positive values indicate possibility of vertical propagation of waves while negative values indicate trapping of waves. Right: the wind speed and direction from the same radiosondes.

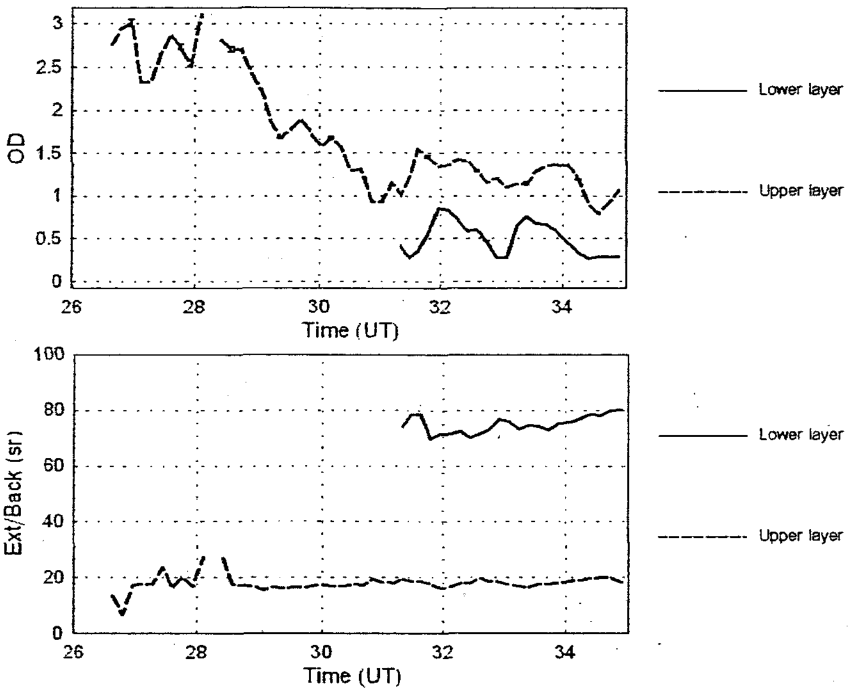

Figure 10: Layer mean optical depth (upper plot) and extinction to backscatter ratio (S) for the two layers observed in figure 7. The S values in the upper cloud layer are quite typical for cirrus clouds, however the much higher values in the lower layer are more consistent with smoke or dust.

the wind analysis indicates the possibility of directional wind shear between the altitudes of 5 and 7 km, a possible explanation for the waves observed in the lower scattering layer between 7-9 km in figure 7 is that waves induced by directional wind shear have propagated vertically to the altitude of the lower scattering layer.

To further investigate the properties of the scattering layers observed in figure 7, the optical depth and layer mean extinction-to-backscatter ratio were calculated and are presented in figure 10. The optical depth of the upper cloud layer varies from a maximum of approximately 3, the rough upper limit of the SRL's ability to quantify optical depth, to approximately 1.0 between approximately 27 and 34 UTC. The lower cloud layer possessed mean optical depth of approximately 0.5. Both of these values are quite consistent with cirrus clouds. However, the extinction to backscatter ratio, S, of the two layers is markedly different. The mean S value in the upper layer of ~20 sr is quite consistent with cirrus cloud values that have been measured using Raman lidar systems previously [Reichardt et. al., 2002] [Whiteman et. al., 2004]. The mean value in the lower layer of ~70-80 is quite atypical of cirrus clouds and more indicative of smoke or absorbing aerosol. The MODIS fire product (http://modis-fire.gsfc.nasa.gov/index.asp) indicated that numerous fires were present in New Mexico, Arizona and California near the path of the three-day back trajectories obtained from the NOAA HYSPLIT model (http://www.arl.noaa.gov/ready/hysplit4.html) analysis at 7, 8, and 9 km, the altitude region of the lower scattering layer seen in figure 7b. Therefore, we take the lower cloud layer to likely consist of hygroscopic smoke particles that have been transported from fires to the west which have served as seeds for ice particle growth.

There is also some indication in the lidar depolarization data that very light precipitation from the cirrus cloud may have helped to seed this lower scattering layer. Figure 11 provides both the volume and particle depolarization measurements of this cloud field. Although there is little indication of cirrus precipitation at 0300 and 0500 UTC below 10 km in the volume depolarization measurements, highly depolarizing precipitation reaching down to ~9.5 km is observed in the particle depolarization measurements. Note also that at the base of the upper cloud layer, the volume depolarization slowly rises to peak values of ~50%

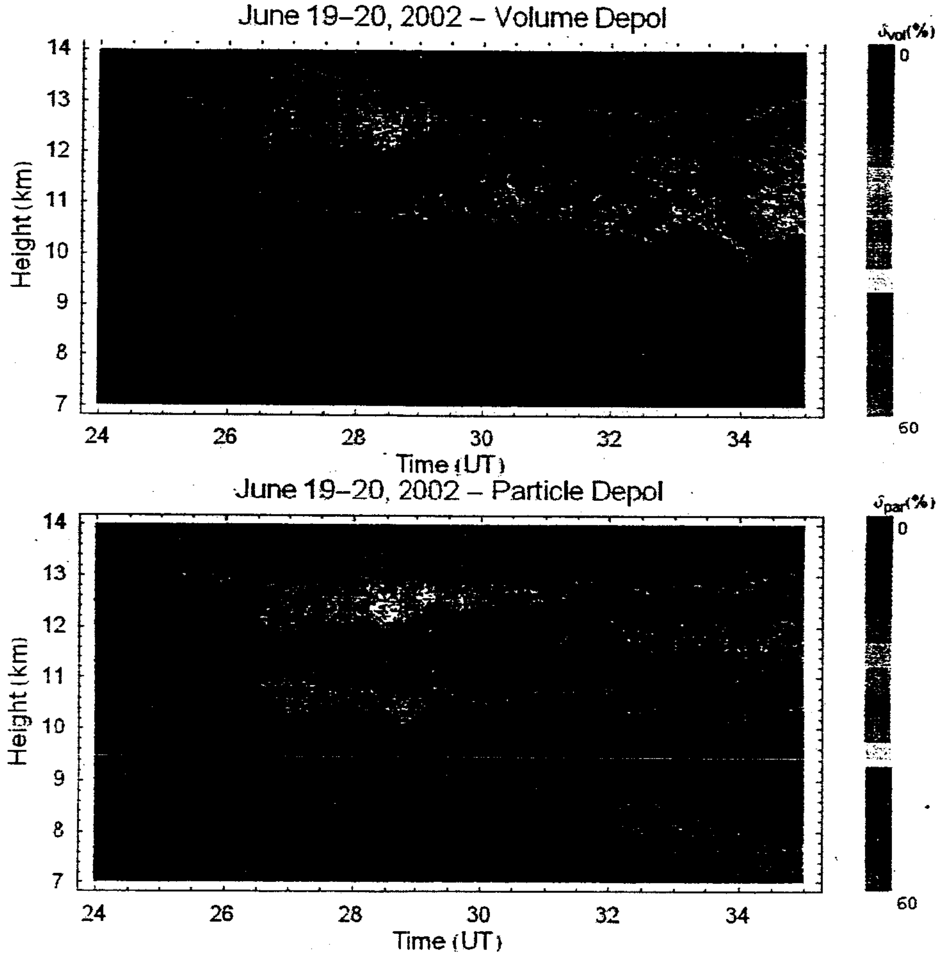

Figure 11: Upper: volume depolarization ratio calculated for the cloud event of June 19-20. Lower: particle depolarization ratio for the same period. The particle depolarization ratio provides a much stronger indication of cirrus precipitation at 27 and 29 UT.

while the particle depolarization ratio indicates ~50% depolarization at the very base of the cloud. The particle depolarization ratio permits the depolarization properties of the particles to be separated from the molecules providing both improved contrast and more accurate characterization of the particles' scattering properties.

5.2.5 Motivation of cirrus cloud modeling study

The cirrus case of June 19-20 presented here is motivating a modeling study at NASA/GSFC with the goal of understanding the physical mechanisms that produce the layering observed in the upper cloud figure 7 that has been interpreted as the cirrus generating region [Lin et. al., 2002]. The simulation of this case through numerical modeling is a considerable challenge. One hypothesis that will be investigated is that radiative cooling is the dominant effect that determines the thickness of the well mixed layer while vertical differential heating between the top and bottom of the cloud destabilizes the layer leading to cirrus precipitation. Previous studies of this type include both 1D [Khvorostyanov et. al., 2001] [Sassen et. al., 2001] [Lin et. al., 2005] and 2D [Luo et. al., 2003] simulations of cloud microphysical properties, which were compared with ground-based measurements. For the case of June 19-20, we will compare the microphysical and optical properties derived from a 2D model with multi-ice-category bin microphysics to the lidar profile measurements of ice water content, particle size and depolarization ratio. To aid this study, the technique for reducing the cross talk between the parallel and perpendicular channels will be optimized and a multiple scattering correction will be applied to the SRL depolarization data.

6 Summary

The NASA/GSFC participated in the first International H_2O Project in May-June 2002. In part I of this paper, the new SRL configuration for IHOP that included measurements of water vapor, aerosol backscatter, extinction, depolarization, liquid water, ice water and temperature was described along with the analysis procedures. In part II, comparisons of the SRL water vapor measurements and those of the LASE airborne DIAL water vapor lidar and the NCAR reference radiosonde were presented. Both comparison indicated good agreement between the sensors up to an altitude of 4 km, the upper limit of the analysis due to the influence of solar background on the SRL water vapor measurements. Daytime and nighttime case studies were presented to illustrate the diurnal measurement capability of the system and to quantify the random errors under these different measurement conditions. The error analysis showed that the system upgrades permitted water vapor to be quantified in the daytime boudary layer with sufficient resolution to permit studies of convective processes. The upgrades also permitted improved upper tropospheric water vapor measurements. This upper tropospheric measurement capability was demonstrated in the context of an evolving cirrus cloud system where humidification due to cirrus precipitation was quantified. Various other aspects of this cirrus cloud case were also studied including cirrus cloud ice water content, particle diameter, optical depth and extinction to backscatter ratio. Oscillations observed in one of the cloud layers were investigated. The conclusion was that smoke particles transported from fires to the west of the measurement site likely served as ice condensation nucleii for the cloud layer. The smoke/ice particles in this layer were induced to oscillate due to vertically propagating waves created below the layer by directional wind shear. There was also some indication in the lidar depolarization measurements that the cirrus precipitation could have helped to seed the lower cloud layer.

7 Acknowledgements

The authors would like to thank the NASA Interdisciplinary Program managed by Dr. Jim Dodge for its support of this activity.

8 References

[Browell and Ismail, 1995] Browell E. V., S. Ismail, 1995: First Lidar Measurements of Water Vapor and Aerosols from a High-Altitude Aircraft, OSA Optical Remote Sensing of the Atmosphere Technical Digest, Vol. 2, 212-214.

[Browell et. al., 1997] Browell E. V., S. Ismail, W. Hall, A. Moore, S Kooi, V. Brackett, M. Clayton, J. Barrick, F. Schmidlin, N. Higdon, S. Melfi, D. Whiteman, "LASE Validation Experiment", Advances in Atmospheric Remote Sensing with Lidar, A. Ansmann and et al., Eds., Springer-Verlag, Berlin, 289-295 (1997).

[Demoz et. al., 2004] Demoz, B et. al., Analysis of a Dryline Case from IHOP.

[Flamant et. al., 2003] C. Flamant, S. Koch, T. Weckwerth, J. Wilson, D. Parsons, B. Demoz, B. Gentry, D. Whiteman, G. Schwemmer, F. Fabry, W. Feltz, M. Pagowski et P. Di Girolamo, 2003 : The life cycle of a bore event over the Southern Great Plains during IHOP_2002, 10th AMS Conference on Mesoscale Processes, Portland, Oregon, June 2003

[Khvorostyanov et. al., 2001]Khvorostyanov, V. I., J. A. Curry, J. O. Pinto, M. Shupe, B. A. Baker, and K.

Sassen, 2001: Modeling with explicit spectral water and ice microphysics of a two-layer cloud system of altostratus and cirrus observed during the FIRE Arctic Clouds Experiments, JGR, 106, 15099-15112.

[Lin et. al., 2002] Lin, R-F, Starr DO, DeMott PJ, Cotton R, Sassen K, Jensen E, Karcher B, Liu XH, 2002: Cirrus Parcel Model Comparison Project. Phase 1: The critical components to simulate cirrus initiation explicitly J. Atmos. Sci., 59, 15, 2305-2329 (2002).

[Lin et. al., 2005] Lin, R.-F., D. O'C. Starr, J. Reichard, P. J. DeMott, Nucleation in synoptically forced cirrostratus, accepted by J. Geophys. Res.

[Linné et. al., 2000] Linné, H., D. D. Turner, J.E.M. Goldsmith, T.P. Tooman, J. Bösenberg, K. Ertel, S. Lehmann, 2000: Intercomparison of DIAL and Raman Lidar Measurements of Humidity Profiles, in Advances in Laser Remote Sensing, selected papers from the 20th International Laser Radar Conference, Vichy France, July 2000. A. Dabas, C. Loth, J. Pelon, Eds.

[Luo et. al., 2003] Luo, Y., S. K. Krueger, G. G. Mace, and K.-M. Xu, 2003: Cirrus cloud properties from a cloud-resolving model simulation compared to cloud radar observations. J. Atmos. Sci., 60, 510-525.

[Melfi et. al., 1989] Melfi, S. H., D. N. Whiteman, R. A. Ferrare, 1989: Observation of atmospheric fronts using Raman lidar moisture measurements, *J. App. Meteor.*, **28**, 789-806.

[Ralph et. al., 1997] Ralph, F. M., P. Newman, T. Keller, D. Levinson, L. Fedor, 1997: Observations, Simulations, and Analysis of Nonstationary Trapped Lee Waves, *J. Atmos. Sci.*, Vol 54, 1308-1333.

[Reichardt et. al., 2002] Reichardt, J., S. Reichardt, A. Behrendt, and T. J. McGee, 2002: Correlations among the optical properties of cirrus-cloud particles: Implications for spaceborne remote sensing, Geophys. Res. Lett., 29, 1029-1032.

[Sassen et. al., 2001] Sassen, K., Z. Wang, V. I. Khvorostyanov, G. L. Stephens, and A. Bennedetti, 2002: Cirrus cloud ice water content radar algorithm evaluation using an explicit cloud microphyhsical model, J. Appl. Meteor., 41, 620-628.

[Scorer 1949] Scorer, R. S., 1949: Theory of waves in the lee of mountains, Quart. J. Roy. Meteor. Soc., 75 , 41-56.

[Senff et. al., 1994] Senff, C., J. Bösenberg, G. Peters, 1994: Mesurement of water-vapor flux profiles in the convective boundary-layer with lidar and RADAR-RASS, J. Atmos. Ocean. Tech., 11 (1): 85-93.

[Shutts, 1997] Shutts, G., 1997: Operational lee wave forecasting, Meteorol. Appl., 4, 23-35.

[Wang et. al., 2003] Wang, J.,Carlson DJ, Parsons DB, Hock TF, Lauritsen D, Cole HL, Beierle K, Chamberlain E, 2003: Performance of operational radiosonde humidity sensors in direct comparison with a chilled mirror dew-point hygrometer and its climate implication Geophys. Res. Lett., 30, 16, 1860.

[Wang et. al., 2004] Wang, Z., D. N. Whiteman, B. B. Demoz, I. Veselovskii, 2004: A new way to measure cirrus cloud ice water content by using ice Raman scatter with Raman lidar, Geophys. Res. Lett., Vol 31, L15101.

[Weckworth et. al., 2004] Weckworth T. M., IHOP, D. Parsons, S. Koch, J. Moore, M. LeMone, B. Demoz, C. Flamant, B. Geerts, J. Wang, W. Feltz, 2004: An Overview of the International H2O Project (IHOP_2002) and Some Preliminary Highlights", Bull. Amer. Meteor. Soc., Feb, 2004, 253-277.

[Whiteman et. al., 1992] Whiteman, D.N., S.H. Melfi, and R.A. Ferrare, 1992: Raman lidar system for the measurement of water vapor and aerosols in the earth's atmosphere", *Appl. Opt.*, **31**, No. 16, 3068-3082.

[Whiteman et. al., 2004] Whiteman, D. N., Z. Wang, and B. Demoz, 2004: Subtropical cirrus cloud extinction to backscatter ratios measured by Raman Lidar during CAMEX-3. Geophys. Res. Lett., doi:10.1029/2004GL020003.

[Whiteman et. al., 2005a] Whiteman, D. N., B. Demoz, P. Di Girolamo, J. Comer, I. Veselovskii, K. Evans, Z. Wang, M. Cadirola, K. Rush, D. Sabatino, G. Schwemmer, B. Gentry, S. H. Melfi, B. Mielke, D. Venable, T. Van Hove, E. Browell, R. Ferrare, S. Ismail, J. Wang, 2005: Raman Water Vapor Lidar Measurements During the International H_2O Project. I. Instrumentation and Analysis Techniques, this issue.

Raman Lidar Measurements during the International H_20 Project. II. Instrument Comparisons and Case Studies – Popular Summary

D. N. Whiteman, B. Demoz, P. Di Girolamo, J. Comer, I. Veselovskii, K. Evans, Z. Wang, D. Sabatino, G. Schwemmer, B. Gentry, R.-F. Lin, E. Browell, R. Ferrare, S. Ismail, J. Wang

The amount of water vapor in the atmosphere helps to determine the likelihood that severe storms may develop. The concentration of water vapor, though, is highly variable in space and time. And yet small changes in water vapor concentration over a short period of time or over a short spatial distance can determine whether a storm may or may not develop. Therefore, in order to improve the ability to forecast severe weather such as thunderstorms it is important to measure water vapor in the atmosphere with high spatial and temporal resolution.

One of the most attractive research tools for measuring water vapor in the atmosphere with high spatial and temporal resolution is a Raman lidar. A Raman lidar consists of a laser transmitter, a telescope receiver and optics and electronics for processing optical and electronic signals. A laser pulse is emitted into the atmosphere and it interacts with molecules in the atmosphere causing them to become excited and to emit, through the Raman process, photons of different wavelength than emitted by the laser. The molecule that emitted these photons can be identified based on the wavelength of the photons emitted. This is the way that a Raman lidar identifies water vapor molecules in the atmosphere.

One of the great challenges in Raman lidar measurements has been to make useful daytime measurements of the water vapor profile under bright daytime conditions. In this second of two papers, we quantify the quality of the daytime water vapor measurements and analysis measurements taken during the daytime and nighttime of water vapor and cirrus clouds.